Preferential Orientation of Crystals Induced by Incorporation of Organic Ligands in Mixed-Dimensional Hybrid Perovskite Films

Rui Wang, Yu Tong, Aurora Manzi, Kun Wang, Zhendong Fu, Emmanuel Kentzinger, Jochen Feldmann, Alexander S. Urban, Peter Müller-Buschbaum*, and Henrich Frielinghaus**

R. Wang, Dr. Z. Fu, Dr. H. Frielinghaus
Jülich Centre for Neutron Science at MLZ
Forschungszentrum Jülich GmbH
Lichtenbergstr. 1
85747 Garching, Germany
E-mail: h.frielinghaus@fz-juelich.de

Dr. E. Kentzinger
Jülich Centre for Neutron Science JCNS
Peter Grünberg Institut PGI
JARA-FIT
Forschungszentrum Jülich GmbH
52425 Jülich, Germany

Y. Tong, A. Manzi, Prof. J. Feldmann, Dr. A. S. Urban
Photonics and Optoelectronics Group
Department of Physics and Center for NanoScience (CeNS)
Ludwig-Maximilians-Universität München
Amalienstr. 54
80799 Munich, Germany
E-mail: urban@lmu.de

R. Wang, K. Wang, Prof. P. Müller-Buschbaum
Lehrstuhl für Funktionelle Materialien
Physik-Department
Technische Universität München
James-Franck-Str. 1
85748 Garching, Germany
E-mail: muellerb@ph.tum.de

Keywords: hybrid perovskite, amplified spontaneous emission, grazing incidence scattering, thin film

Abstract: Organic-inorganic perovskites demonstrate great potential for optical applications due to their intriguing optical and optoelectronic properties. Dedicated efforts have been carried out to understand the energy landscape and charge carrier mobilities for perovskite

materials. In order to further boost these materials toward large-scale applications, an alternative "bottom-up" route for the understanding about correlation between the morphology of high-quality planar films and its optical properties is essential. Here, mixed dimensional bromide-based hybrid perovskite thin films are prepared from a simple one-step solution processing route using mixtures of methylammonium bromide (MABr) and octylammonium bromide (OABr). Grazing incidence scattering (GIS) data statistically reveals that the development of thin film morphology as well as crystal orientation depends on the orientation of the OABr crystallites. Our study opens up further insight into the morphology of perovskite thin films. In combination, the occurrence of amplified spontaneous emission (ASE) in perovskite films with low ASE thresholds with values approaching 17.8 $\mu J/cm^2$ is demonstrated and appears to be closely correlated to the tailored morphology, highlighting its importance for realizing optical gain media.

1. Introduction

Metal halide hybrid perovskite materials (ABX_3, A = methylammonium (MA) or formamidinium (FA); B = Pb^{2+}, Sn^{2+}; X = Cl^-, Br^- or/and I^-) have gained tremendous attention in particular in the photovoltaics community in the past six years.[1] Their large absorption coefficient as well as long carrier diffusion length promote an unprecedented efficiency boost of hybrid perovskite-based solar cells with record device efficiency values above 22%.[2] Moreover, hybrid perovskite materials also exhibit a high photoluminescence quality (full width half maximum, FWHM ≈ 20 nm), a continuously tunable band structure to cover the entire visible light spectrum, a high photoluminescence quantum yield, and a small capture cross-section of trap states.[3,4] These intrinsic advantages have manifested hybrid perovskite materials as versatile candidates not only for photovoltaics but also as light emitting and gain media.[5]

The first report about hybrid perovskite thin films exhibiting amplified spontaneous emission (ASE) at room temperature dates back to the year 2014.[4] A low ASE threshold fluence of I_{ASE} = 12 ± 2 μJ/cm^2 was obtained for 65 nm thick 3D $MAPbI_3$ perovskite thin films. This value is comparable to state-of-art gain media comprising organic polymers, e.g. poly (9,9-dioctylfluorene):poly (para-phenylenevinylene) derivative "Super Yellow" ($F8_{1-x}$:SY_x) with I_{ASE} = 14 μJ/cm^2, or colloidal quantum dots (e.g., CdSe/CdS@CdS core/crown@shell heterostructured nanoplatelets, I_{ASE} ≈ 20 μJ/cm^2).[6] Stranks et al. achieved an even lower ASE threshold fluence of ≈ 7.6 μJ/cm^2 by stacking $MAPbI_3$ thin films within a cholesteric-liquid-crystal (CLC) in combination with a gold back-reflector.[7] Recently, Tong et al. reported a new ultrasonication synthesis path to fabricate all inorganic perovskite nanocrystals with considerably lower ASE thresholds, on the order of only 2 μJ/cm^2, which shows the potential for large-scale production.[8] The outstanding low ASE threshold gave impetus to use halide perovskites in light-emission applications. Moreover, the use of solution processable fabrication routes makes perovskite materials suitable for a cost-efficient production and enables an applicability to flexible optoelectronic devices.[9]

In the present work, we demonstrate succinctly one-step solution-processed mixed dimensional (coexistence of three-dimensional (3D) bulk crystals and two dimensional (2D) Ruddlesden-Popper crystals) perovskite thin films, which exhibit relatively low optically pumped ASE thresholds. A schematic illustration of low dimensional perovskite platelets with different thickness is given in Figure S1 in the Supporting Information (SI). A long organic molecule, octylammonium bromide (OABr) is mixed with methylammonium bromide (MABr) during the synthesis. This fabrication path is similar to the method used for the fabrication of perovskite nanoplatelets, wherein the OABr, which is too large to be incorporated into the crystal structure, leads to a termination of the crystal growth instead.[10] In contrast to the earlier work, in our approach a moderate concentration of the long organic chain (OABr) has the function of enhancing the quality of the thin film by controlling the

morphology. We compare three samples with varying OABr content, hereafter abbreviated as PeOA10 (10%), PeOA20 (20%) and PeOA40 (40%), with the number referring to the mole ratio of the OABr over the total organic salts. In addition, samples using neat MABr (0% OABr, PeOA0) and neat OABr (100% OABr, PeOA100) are prepared for comparison. In comparison to previous reports,[11] we focus on a "bottom-up" approach towards a systematic understanding of the thin film morphology for obtaining better optical properties. Combining different grazing incidence scattering (GIS) techniques, we analyze the morphology of the mixed-dimensional hybrid perovskite thin films from micrometer scale domain structures down to the atomic level crystal orientation. GIS has been proven to be a unique technique for the structural characterization of polymer and hybrid perovskite thin films.[12] For example, it was reported that the preferential orientation degree of perovskite crystals has a direct impact on the efficiency of charge transportation and collection.[13] In contrast, the understanding of the relationship between crystal orientation and optical quality is still limited for hybrid perovskite gain media. In the present work, we observe that the degree of perovskite crystal orientation is correlated to the ASE thresholds in mixed-dimensional hybrid perovskite thin films. A low ASE threshold below 18 $\mu J/cm^2$ is realized for well-oriented crystal domains. The understanding of the orientation of the perovskite crystals in thin films can serve as an excellent basis for the realization of high quality gain media.

2. Result and Discussion

A schematic illustration of the one-step sample preparation route is shown in Figure 1a. All precursors (MABr, OABr, and $PbBr_2$) are mixed in N,N-Dimethylformamide (DMF) solvent under ambient atmospheric conditions. Films of the mixed dimensional hybrid perovskite with a thickness around 170 nm are prepared by spin-coating under argon atmosphere. No additional solution washing is applied in contrast to previous reports.[14a,14d] After film deposition a thermal treatment is used to remove residual solvent and hence improve

perovskite crystallization.[15] It is worth emphasizing that the complete sample preparation time from precursor weighing until the finalization of thin films takes only about 1 hour, which makes this route highly interesting for applications. Figure 1b sketches a representative experimental set-up used for grazing incidence scattering (GIS). Typically, the X-ray or neutron beam impinges on the sample surface under a very shallow incident angle α_i (e.g. < 1°), whereas the scattered intensities are recorded with a two-dimensional (2D) detector with different exit angles α_f and out-of-plane angles ψ. Transferred into reciprocal space for a full quantitative analysis, the obtained scattering vector is

$$\vec{q} = \overrightarrow{k_f} - \overrightarrow{k_i} = \begin{pmatrix} q_x \\ q_y \\ q_z \end{pmatrix} = \frac{2\pi}{\lambda} \begin{pmatrix} \cos(\alpha_f)\cos(\psi) - \cos(\alpha_i) \\ \cos(\alpha_f)\sin(\psi) \\ \sin(\alpha_i) + \sin(\alpha_f) \end{pmatrix} \quad (1)$$

It depends on the angles α_i, α_f and ψ. In a practical GIS experiment the 2D detector is placed either close to the sample (called grazing incidence wide angle scattering, GIWAS) or a few meters from the sample position (called grazing incidence small angle scattering, GISAS), depending on the desired range of the scattering vector and consequently feature size.[12a,12d] By combining GIWAS and GISAS all relevant length scales in hybrid perovskite thin films can be addressed.[12e]

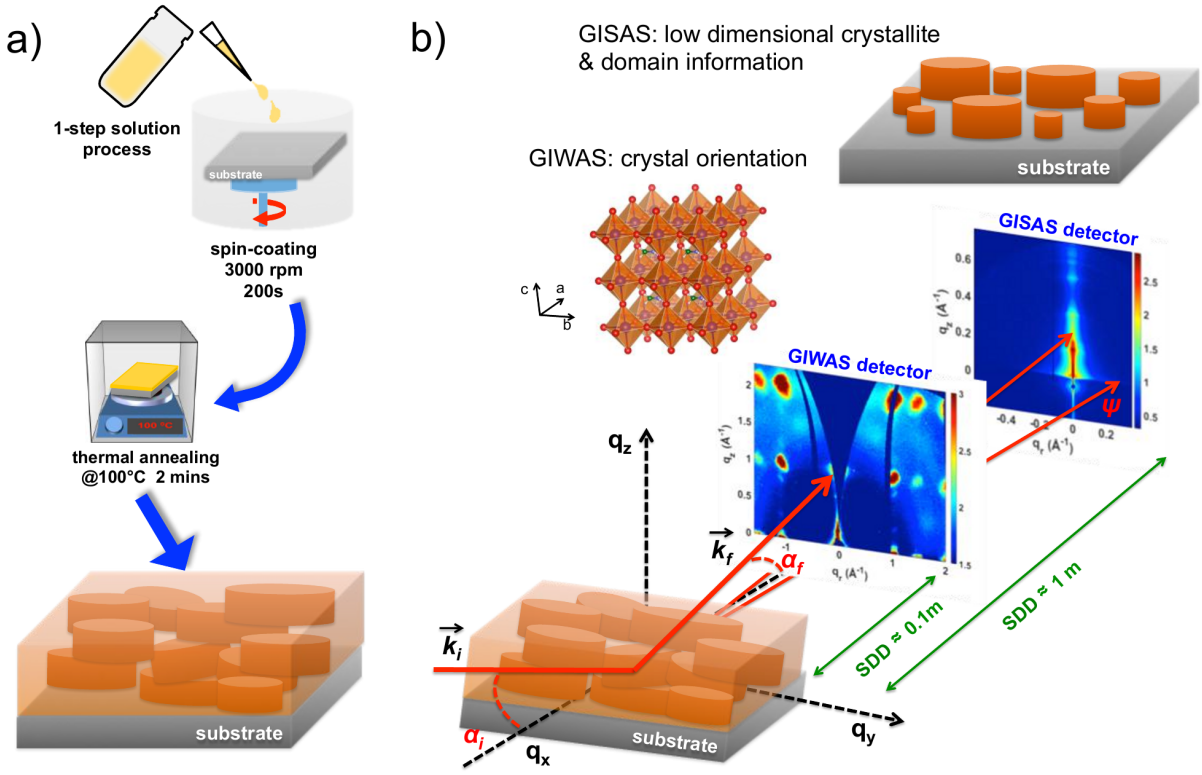

Figure 1. Schematic representation of (a) the one step solution-processed sample preparation route and (b) the GIS set-up. The incidence angle is α_i, the exit angle is α_f and the out-of-plan angle in the $\mathbf{q}_y$ direction is ψ. By applying different sample-detector-distances (SDD), both hybrid perovskite crystal orientations on the atomic length scale and domain structures in sub-micrometer scale can be examined.

The surface morphology of the hybrid perovskite thin films is characterized with scanning electron microscopy (SEM) and with atomic force microscopy (AFM). If no OABr is used in the sample preparation (sample PeOA0), no homogeneous perovskite films can be achieved as seen in Figure S2a in the SI. Only micrometer-sized isolated $MAPbBr_3$ crystals with poor interconnection are found, which corroborates previous reports that it is relatively hard to achieve a full surface coverage for $MAPbBr_3$ films by using a one-step normal solution spin coating deposition from neat DMF solvent.[14] When using OABr the film quality is improved and homogeneous films can be realized. As seen in Figure 2a-2c the OABr content alters the film morphology. Uniform domains on the scale of tens of micrometers are formed in the PeOA10 sample (Figure 2c). The average domain size decreases remarkably with increasing OABr content. For the PeOA40 sample gaps appear on the film surface and the film uniformity is reduced. The AFM images (Figure 2d-f) complementarily highlight the strong

impact of the OABr content on the local morphology of the films. The micrometer scale domains of the PeOA10 sample are composed of hundred nanometer sub-structures (Figure 2f) and a thin layer can be noticed on the domain surfaces. At larger magnification, layered-like structures can be seen clearly in PeOA10 and formed aggregates at higher OABr concentrations, the height of which seems to increase with increasing OABr content (Figure S3 in SI).

To get information about the inner morphology of the films with a high statistical relevance, the films are probed with grazing incidence small angle neutron scattering (GISANS) and grazing incidence small angle X-ray scattering (GISAXS) for an understanding of domain morphology on both the mesoscale and nanoscale, respectively. The horizontal line cuts of the 2D GISANS and 2D GISAXS data are displayed in Figure 2g and Figure 2h, respectively. The scattering curves obtained from the GISANS measurements exhibit a power law scattering ($I(q) \propto q_y^{-\alpha}$) in the middle q_y range (0.01-0.05 nm^{-1}), corresponding to the mesoscale (80-300 nm, Figure S4b, see SI), reflecting the characteristics of mass fractals ($2 < \alpha < 3$) for all three samples.[16a,16b,17a] The mass fractal reveals a self-similar packing of domains as schematically illustrated in inset of Figure 2g.[16c] In a previous report the fractal morphology of $MAPbI_3$ films was explained by a fractal-like diffusion of MAI into PbI_2 films.[17b] Based on these findings we estimate that the mass fractal morphology on the hundreds nanometer scale is formed by grain aggregation with the presence of voids in the films. The value of the exponent can give an estimate of the compactness of the perovskite domain arrangement, with a lower value corresponding to a less dense film.[18] For the PeOA20 and PeOA40 samples, the value of the exponent (α) is smaller than for the PeOA10 sample, which indicates the presence of a less dense film for higher OABr content, concomitant with our observations from the AFM topography images. In Figure 2h, clear variations in the scattering curves are revealed on the nanoscale (2-25 nm). A prominent

shoulder-like intensity distribution at $q_y \approx 0.3$ nm^{-1} is visible in sample PeOA10, originating from the correlated domain structures on the size order of 5 to 10 nm (Figure S5a, see SI). Upon increasing the OABr content, the shoulder becomes significantly less prominent in sample PeOA20 and vanishes completely in sample PeOA40. The degree of morphological order in the investigated system determines the shape of the scattering peak.[19] A system possessing a higher degree of order exhibits a more prominent scattering feature. Therefore, the uniformity of the resulted nanoscale domain structures is less developed in sample PeOA40 with respect to that in sample PeOA10. In addition, the scattering curve of sample PeOA10 contributes a mass fractal with dimension $\alpha \approx 2.7$ in the low q_y range (>0.3 nm^{-1}), which is the same value obtained from the GISANS data (Figure 2g). The exponents extracted from the different q ranges from the scattering curve of sample PeOA20 reveal that in the low q_y range the samples are dominated from platelets (exponent $\alpha = 2.1$), whereas in the high q_y range (<0.3 nm^{-1}), the domains tend to form rod-like aggregates instead, as described by the exponent $\alpha = 1.1$.[16b] In the PeOA40 with the highest OA content, the scattering curve displays a uniform q_y^{-2} power law scattering, indicating the domain structures over the size range of 2 to 22 nm are dominated by platelet-like structures (see Figure S5a).[16b]

Caused by the changes in the film morphology, the variation of the OABr content affects the optical properties of the mixed-dimensional perovskite films, as evidenced by UV-Vis and PL-spectroscopy (Figure 2i and Figure 2j). The bulk-like $MAPbBr_3$ reference sample PeOA0 shows the familiar absorption onset at 525 nm and a corresponding PL peak at 535 nm.[10] In the case of OABr-based crystals $(OA)_2PbBr_4$, a steep absorption edge at 396 nm and a corresponding PL peak at 405 nm are observed, likely corresponding to excitons formed inside the thin $(OA)_2PbBr_4$ sheets.[20a] For all of the samples containing mixtures of OABr and MABr used in the present study, the absorption onset is slightly blue-shifted from the typical bulk value to ~ 510 nm due to the onset of weak quantum confinement,[20b] while the PL

maxima remain roughly at the same position. A closer inspection of the absorption spectra, however, reveals additional features at 472 nm, 451 nm, and 433 nm, which are not present in the bulk-like reference sample. These correspond well to values obtained for 2D platelets with thicknesses down to a single perovskite unit cell.[10,21] These peaks become more prominent as the OABr content is increased. Simultaneously, when magnifying the short wavelength regions on the PL spectra of the PeOA10 and PeOA20 samples, distinct peaks become visible at the same positions as the PL peaks obtained for the aforementioned perovskite nanoplatelets. In the PeOA40 sample these peaks are so prominent that they can be seen in the PL spectrum without the need to magnify the short wavelength region. The comparison of the intensities of the UV-Vis absorption spectra and of the PL peaks, suggests that for the samples with low content of OABr, energy transfer from the thinner nanoplatelets to the bulk crystals is quite efficient, as evidenced by the weak PL peaks. This is further supported by PL-excitation (PLE) measurements. Emission from the 2D platelets is clearly seen in the PLE spectrum of the PeOA10 sample (see Figure S4a and Figure S9). However in the PeOA40 sample, the PL peaks are quite prominent, likely due to the fact that in this sample, the domains are separated by larger gaps, hindering energy transfer.[22] Additional measurements showed the quantum yields in all samples to be rather low, with values below 2% (cf. Table S2) and increased upon increasing the OABr content. PL lifetime measurements on the other hand reveal a strong correlation with OABr content, as the PL lifetime significantly decreased with increasing OABr content (see Figure S8, Table S2). A determination of decay rates, as previously done for perovskite nanocrystals, is however not possible due to the dimensionally inhomogeneous in samples.[25]

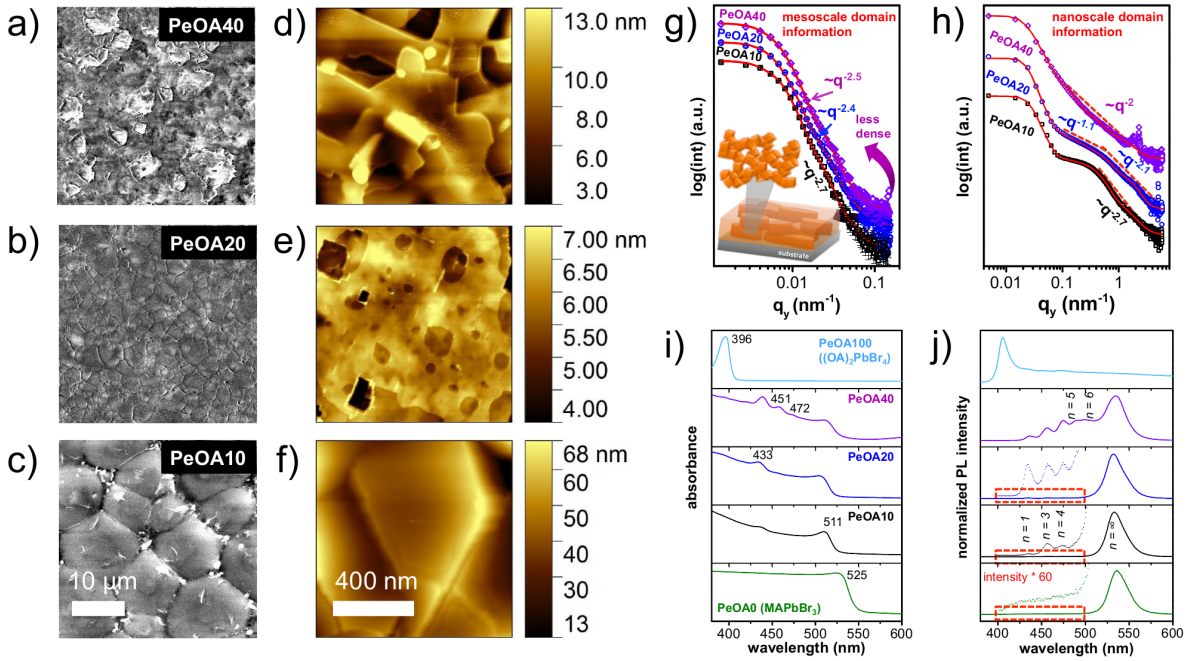

Figure 2. SEM top-view images (scale bar 10 µm) of the mixed dimensional hybrid perovskite films with a) 40% (PeOA40), b) 20% (PeOA20) and c) 10% (PeOA10) mole ratio of OABr. The AFM topography images (scale bar 400 nm) follow the same sample order (d: PeOA40, e: PeOA20, f: PeOA10). Horizontal line cuts of the g) 2D GISANS and h) 2D GISAXS data (symbols) of the three perovskite films and corresponding fits (solid lines). A detailed description about the GISANS/GISAXS data analysis can be found in the SI. A representative mass fractal morphology is shown in the inset. i) UV-Vis and j) PL-spectra of the perovskite films. Peak positions are highlighted in images and the low dimensional perovskite platelets are indexed in PL-spectra in terms of $MAPbBr_3$ unit cell thickness (n).

X-ray diffraction (XRD) data confirm that all films consist of $MAPbBr_3$ crystallized in a cubic crystal structure (Figure 3a). Since most reflections originate from the (001) family, a high degree of crystal orientation is suggested.[20b] Additional features appear at low q values ($q < 1$ Å^{-1}) for the OABr-containing samples, either due to residual precursor ($PbBr_2$, OABr) or due to the formation of 2D platelets, e.g. $(OA)_2PbBr_4$.[20a] To further study the crystal orientation and quality of the mixed-dimensional perovskite films, we perform grazing incidence wide angle and small angle X-ray scattering (GIWAXS and GISAXS) measurements. The 2D GIWAXS data and the 2D GISAXS data are shown in Figures 3b-3d and Figures 4a-4c (q_z is the component of the scattering vector perpendicular to the sample surface and $q_r = (q_x^2+q_y^2)^{½}$ is the component of the scattering vector parallel to the substrate), respectively. To compare GIWAXS with XRD the 2D GIWAXS data are integrated (Figure

3e). The resulting Bragg peak positions are in agreement with those seen in the XRD data. Differences arise from the fact that XRD accesses Bragg peaks along the surface normal (q_z direction), which is partly inaccessible by GIWAXS, whereas GIWAXS probes in-plane Bragg peaks, e.g. arising from the (101) plane of the cubic perovskite phase, being inaccessible with XRD.

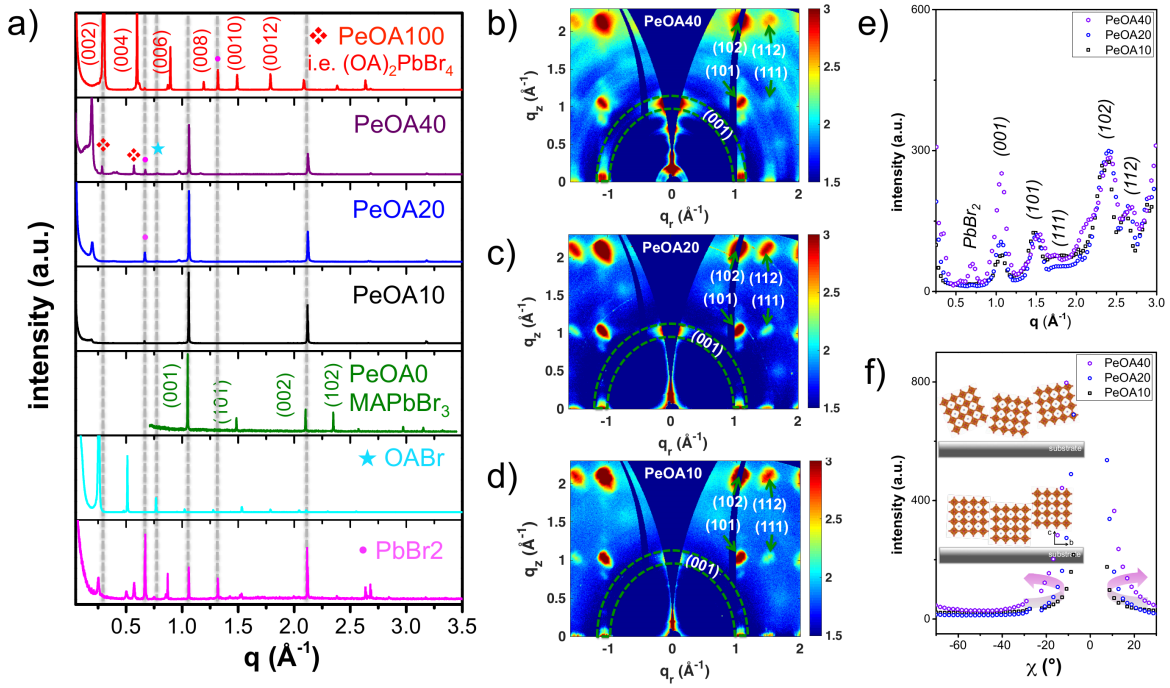

Figure 3. a) XRD patterns of perovskite films with varying mole ratio% of OABr as indicated. XRD patterns of pure MABr based 3D bulk $MAPbBr_3$ crystal (sample PeOA0), pure OABr based 2D crystal $(OA)_2PbBr_4$ (sample PeOA100), OABr and $PbBr_2$ are showed for comparison. GIWAXS data of the perovskite films with OABr mole ratio of: b) 40% (PeOA40), c) 20% (PeOA20) and d) 10% (PeOA10), respectively. e) Integrated intensity profiles from 2D GIWAXS data. f) Azimuthal intensity integrations of the (001) Bragg peaks of 3D perovskites at q = 1.06 Å^{-1} and schematic illustration of the different orientations depicted as inset.

All 2D GIWAXS data show intense Bragg peaks at $q > 1$ Å^{-1}, suggesting the presence of 3D bulk $MAPbBr_3$ crystals with a strong preferential orientation, instead of frequently observed intensity rings, indicative of a random crystal orientation. The 3D bulk $MAPbBr_3$ crystals are oriented with the (001) planes parallel to the substrate surface. Thus, charge carriers should be able to diffuse efficiently between 3D $MAPbBr_3$ crystals since a lower number of defects are

likely to form at the grain boundaries.[23] However, the intensity of the (001) Bragg peaks gradually spreads along azimuthal angles (χ) for higher OABr content, resembling a decrease in orientational order. For quantification azimuthal intensity integration of the (001) Bragg peaks is done (Figure 3f). An increase in intensity is observed up to $\chi \approx \pm 30°$ for samples with increasing OABr content, caused by a slight deviation in the orientation of a minor fraction of the 3D crystals. Stronger signals for scattering angles of $q < 1$ Å^{-1} likely stem from higher Bragg peak intensities from 2D perovskite platelets and unreacted precursors and increase with increasing OABr content, in good agreement with the findings from the XRD measurements. A detailed inspection of the GIWAXS data reveals that the amount of 2D platelets increased by a factor of 2 in the sample PeOA40 in comparison with the sample PeOA10 (see Figure S7 in SI).

The 2D GISAXS data (Figures 4a-4c) show intense peaks at $q_z = 0.19$ Å^{-1}, $q_z = 0.23$ Å^{-1} and $q_z = 0.39$ Å^{-1} which correspond to lattice d-spacings of 33.1 Å, 27.3 Å and 16.1 Å, respectively. These can be attributed to 2D platelets with a perovskite unit cell thickness of n= 3, 2 and 0, respectively.[10,21b] A cartoon illustrating 2D platelets of different unit cell thicknesses is shown in the SI (Figure S1). This result corroborates the spectroscopic results presented in Figure 2h and Figure S3 (see SI). The absence of Bragg peaks along the q_r direction for the PeOA10 sample (Figure 4c) indicates that the 2D platelets are highly orientated parallel to the substrate surface, exactly like the 3D bulk $MAPbBr_3$ crystals. At $q_z > 0.5$ Å^{-1}, the scattering patterns are dominated by three intense peaks, originating from $(OA)_2PbBr_4$ ($q_z = 0.59$ Å^{-1}), $PbBr_2$ ($q_z = 0.67$ Å^{-1}) and OABr ($q_z = 0.72$ Å^{-1}),[20a] meaning that both 2D platelets as well as residual precursors crystallize along the surface normal direction. In contrast, at higher OABr content the signals corresponding to the Bragg peaks of the 2D platelets (n = 3, 2) and OABr are observed for an increasing range of azimuthal angles (Figure 4b and Figure 4a). This is further investigated by azimuthal integration around the scattering angles $q = 0.72$ Å^{-1}, $q = 0.67$ Å^{-1} and $q = 0.19$ Å^{-1}, corresponding to the respective diffraction rings of OABr,

$PbBr_2$ and 2d platelets (n = 3). These three Bragg peaks are chosen because they exhibit a strong intensity and since they are not obscured by higher order reflections in the large *q* range.

In Figure 4e, the results from such azimuthal integration show that the OABr crystals are highly oriented parallel to the substrate in the sample PeOA10. Such an orientation could suppress growth along the surface normal, favoring growth of the perovskite crystals along the in-plane direction consequently resulting in the formation a full surface coverage with a large grain size. In contrast, at an OABr content of 40%, an additional strong preferential orientation appears at $\chi \approx \pm 20°$, indicating a partial reorientation of OABr crystallites. Similar intensity features appear at around $\chi \approx \pm 20°$ for the 2D perovskite platelets (n = 3) (Figure 4g). For $PbBr_2$ no similar trend could be observed (Figure 4f). It seems as though both the 3D (Figure 3f) and 2D (Figure 4g) perovskite crystals orient themselves alongside the OABr crystallites. Provided that the long alkyl chain OABr can only fit either in the periphery of the corner-sharing $[PbBr_6]^{4-}$ octahedra or adsorb at the perovskite crystal surface,[21b] we speculate that during crystal formation an isotropically orientated OABr sheet will provide more channels for precursor intercalation and as a consequence the crystal orientation conditions diversify. In comparison to the epitaxial growth of quantum dots in perovskite crystals, which exhibit good crystalline coherence,[24a] we speculate that the multi-dimensional perovskite crystals in our study are self-assembled from solution.[24b]

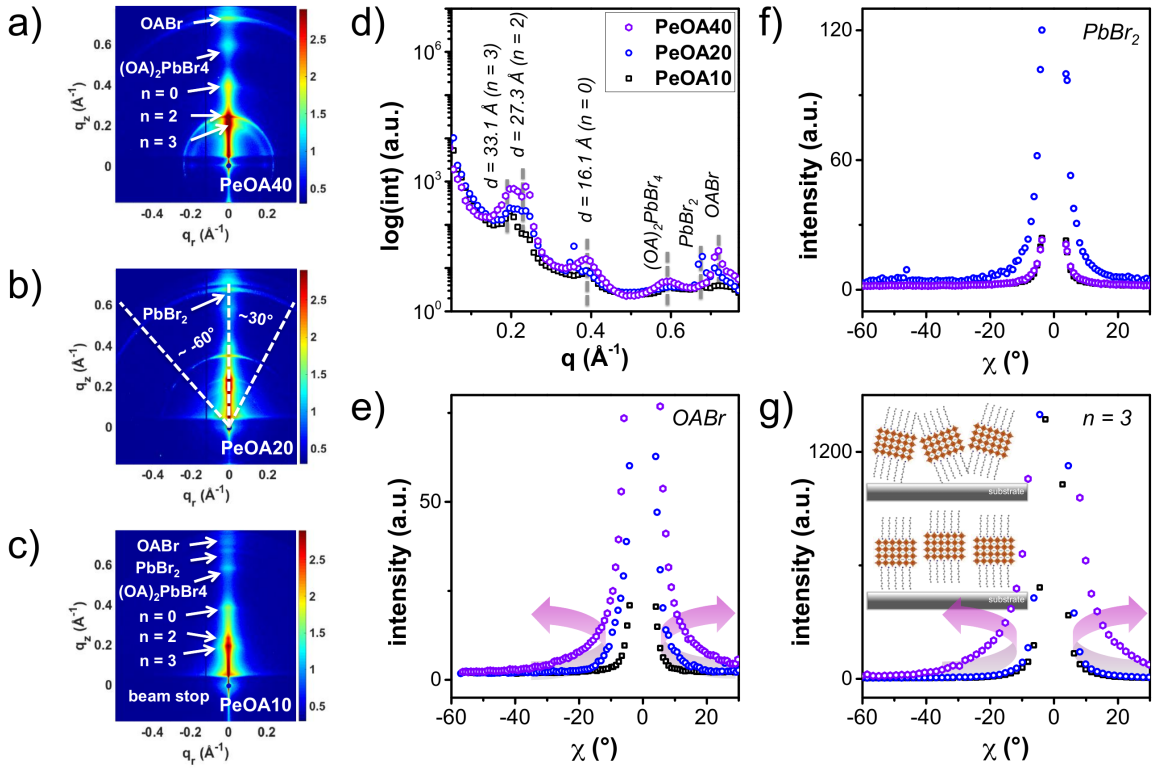

Figure 4. GISAXS data of perovskite films with OABr mole ratio of: a) 40% (PeOA40), b) 20% (PeOA20) and c) 10% (PeOA10). d) Integrated intensity profiles from 2D GISAXS data. Azimuthal integrations of intensity through Bragg peaks at e) q = 0.72 $Å^{-1}$ for OABr, at f) q = 0.67 $Å^{-1}$ for $PbBr_2$ and at g) q = 0.19 $Å^{-1}$ for 2D platelets with four unit cells thickness (n = 3). A schematic illustration of the resulting crystallites orientation variation is shown in the inset of (g).

Lastly to investigate the effect of the organic ligands on the optical quality of the resulting films, we pumped at high laser powers to induce amplified spontaneous emission (ASE) (Figure 5). At low laser fluences the PeOA10 sample shows the typical PL spectrum centered at 530 nm (Figure 5a). As the fluence increases over 15 $\mu J/cm^2$, a second peak, significantly narrower (4.1 nm compared to the 14.5 nm of the low fluence PL peak) emerges as a shoulder at 548 nm. This peak, initially rapidly gains in intensity with respect to the original peak, until it is several times larger. This effect corresponds to the emergence of amplified spontaneous emission. To investigate the threshold of ASE the areas under the respective PL peaks are integrated as well as the total emission spectrum and plotted with respect to the laser fluence (Figure 5b). There is a clear kink in the total area (SE+ASE) at 17.8 $\mu J/cm^2$, indicating the

threshold of ASE. The signal from the ASE rapidly increases until it surpasses the spontaneous emission intensity for fluences of over 25 μJ/cm^2. A similar behavior can be seen for the PeOA20 sample (Figure 5d), with the threshold shifting slightly to higher fluences (Figure 5e). For an even higher OABr content of 40%, no ASE signal could be observed despite the laser fluence being increased to ten times the maximum value used for the other samples (Figure 5g and Figure 5h). The ASE threshold thus seems to be correlated with the content of the organic ligand. However, the mixed-dimensionality of the perovskite crystals in the thin films does not allow us to exclude the presence of additional factors that could play a role in this process, such as energy transfer between different domains and carrier confinement in smaller crystals. For example, PLE measurements suggest that non-radiative energy transfer from nanocrystals exhibiting quantum-confinement to bulk-like crystals is more efficient in the samples with the low OABr content, possibly due to a higher proximity of the crystals (Figure S4 in SI). Additionally, due to the increased amount of quantum confined 2D platelets for high OABr content films (Figure S7 in SI) and the large amount of pinholes, a photon travelling through the film is speculated to interact with less crystals. The higher order of orientation leads to a higher total crystal density, which could also modify radiative and non-radiative recombination rates. Power-dependent measurements conducted on the samples did not result in any observation of Auger recombination, another possible non-radiative decay channel (see Figure S10 in SI). As the control of these parameters is not possible individually, the disentanglement of these processes lies outside the scope of this manuscript.

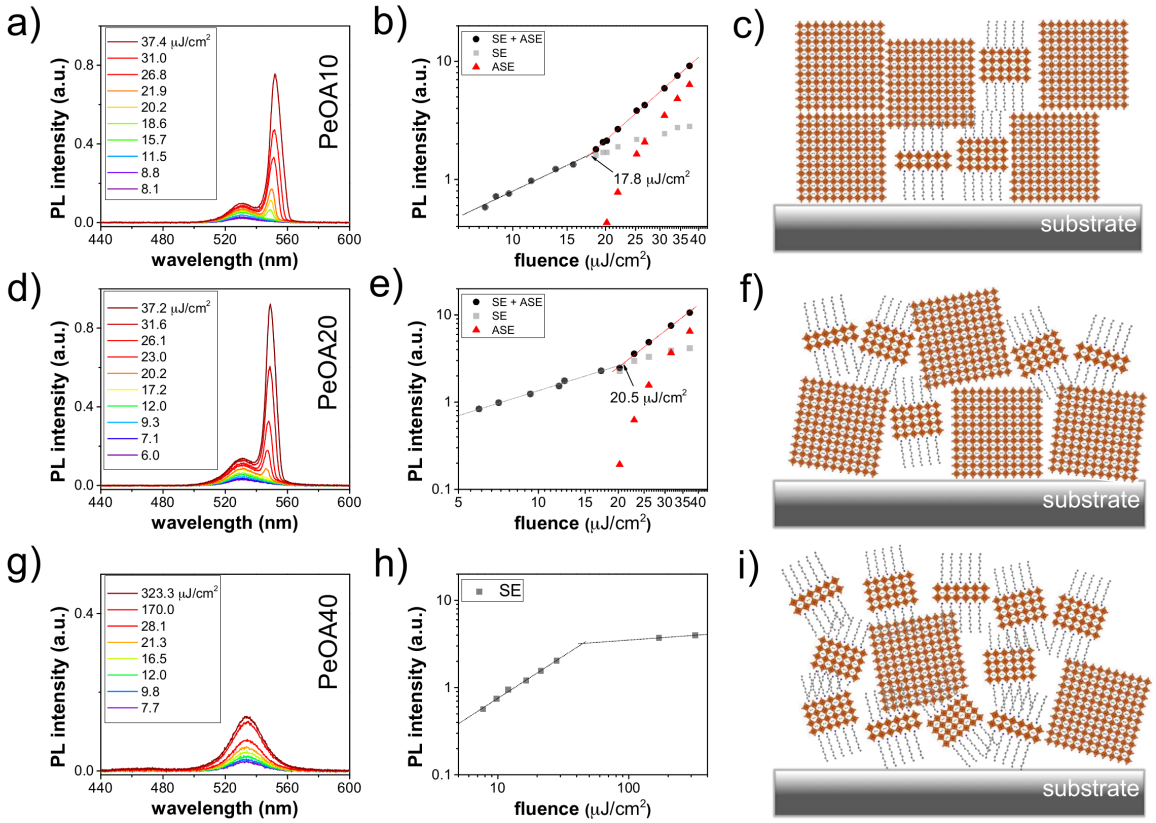

Figure 5. Pump fluence-dependent emission spectra of a) sample PeOA10, d) sample PeOA20 and g) sample PeOA40. The log-log plots of the integrated PL intensity as a function of the pump excitation fluence of b) sample PeOA10, e) sample PeOA20 and h) sample PeOA40. Schematic illustration of the resulting morphology in c) sample PeOA10, f) sample PeOA20 and i) sample PeOA40.

In summary, we present mixed-dimensional hybrid perovskite films prepared via a simple one step solution processing route which exhibit desirable optical gain properties. The perovskite crystal orientation can be effectively tuned by varying the OABr content. A dense film with perfectly oriented crystals is achieved in sample containing 10% mole ratio of OABr without using additional solution washing or any additives. PL lifetime is revealed to diminish alongside the loss in film compactness as well as crystal preferential orientation. Low ASE thresholds are demonstrated for the perovskite films, with the ASE threshold correlating with the content of organic ligands used in the preparation. These films can form the basis for realizing high-quality films for optical gain media in the future.

Experimental Section

Fabrication of Mixed Dimensional Hybrid Perovskite Films: Methylammonium bromide (MABr) and $PbBr_2$ were purchased from Dyesol and Sigma-Aldrich, respectively. Octylammonium bromide (OABr) was prepared by addition of HBr to octylamine in ethanol, following with completed crystallization in a rotary evaporator. The precursors were individually dissolved in dimethylformamide (DMF) at 80 °C with fixed total concentration of MABr (1.67 M), OABr (1.67 M) and $PbBr_2$ (1 M). The mole ratio between organic and inorganic reagent was kept as 1:1, but tuning %OABr content. Mixed dimensional perovskite thin films were spin-coated on acidic pre-cleaned substrates. A 2 minutes post thermal treatment under 100 °C was applied to improve the perovskite crystallization.

Sample Characterization: SEM images were taken with a Gemini Ultra Plus field emission scanning electron microscope with an electron accelerating voltage of 3 kV and a working distance of 1 mm. AFM topography images were obtained with Keysight 5500 Scanning Probe Microscope in intermittent contact mode in air. A pyramidal-shaped silicon tip with a radius of around 8 nm was mounted on the cantilever.

XRD measurements were conducted using a BRUKER D8 ADVANCE diffractometer with an 8 keV Cu-K_α X-ray source. GISANS measurements were performed at KWS-3 at MLZ (Maier-Leibnitz Zentrum), Garching, Germany.[26] A neutron wavelength of 12.8 Å and a sample detector distance of 1.24 m were operated. GIWAXS measurements were carried out using a in-house Ganesha 300XL SAXS-WAXS instrument with an 8 keV Cu-K_α X-ray source. GISAXS measurements were performed at GALAXI diffractometer at JCNS.[27] A Dectris Pilatus 1M detector combined with a BRUKER AXS Metaljet X-ray source were used. An incident angle of 0.4° was applied for both GIWAXS and GISAXS measurements.

ASE measurements were performed at room-temperature using 400 nm femtosecond pulsed laser with a pulse width of 100 fs and a repetition rate of 1KHz.

The UV/Vis absorption spectra were taken with a PerkinElmer UV/Vis spectrometer Lambda 35 in Transmission geometry. The photoluminescence spectra were measured using a Fluorolog-3 FL3-22 (Horiba Jobin Yvon GmbH) spectrometer equipped with a water-cooled R928 PMT photomultiplier tube mounted at a 90° angle. Absolute quantum yields of the perovskite films were measured with an integrating sphere embedded in the spectrometer. The photoluminescence excitation measurements were acquired by using the same instrument as for PL measurement. Spectra were recorded by detecting at 560 nm. Time-resolved fluorescence measurements were performed using a monochromater (Princeton Instrument) equipped time-correlated single photon counting (TCSPC) system (PicoQuant PicoHarp 300). Excitation power dependent PL lifetime measurements were carried out with a steak camera (Hamamatsu C5680). Attenuate filters were used to define the excitation power density whereas samples were excited at 405 nm.

Supporting Information
Supporting Information is available from the Wiley Online Library or from the author.

Acknowledgements
This work was supported by funding from the Excellence Cluster “Nanosystems Initiative Munich” (NIM), the Center for NanoScience (CeNS), by LMU Munich‘s Institutional Strategy LMUexcellent within the framework of the German Excellence Initiative, and by the Bavarian Collaborative Research Project “Solar Technologies Go Hybrid" (SolTech). Y.T and K.W. acknowledge the China Scholarship Council (CSC).

Received: ((will be filled in by the editorial staff))
Revised: ((will be filled in by the editorial staff))
Published online: ((will be filled in by the editorial staff))

References

[1] a) M. M. Lee, J. Teuscher, T. Miyasaka, T. N. Murakami, H. J. Snaith, *Science* **2012**, *338*, 643; b) M. Liu, M. B. Johnston, H. J. Snaith, *Nature* **2013**, *501*, 395; c) J. Burschka, N. Pellet, S.-J. Moon, R. Humphry-Baker, P. Gao, M. K. Nazeeruddin, M. Grätzel, *Nature* **2013**,

499, 316; d) N. Arora, M. I. Dar, M. Hezam, W. Tress, G. Jacopin, T. Moehl, P. Gao, A. S. Aldwayyan, B. Deveaud, M. Grätzel, M. K. Nazeeruddin, *Adv. Funct. Mater.* **2016**, *26*, 2846.

[2] a) Q. Dong, Y. Fang, Y. Shao, P. Mulligan, J. Qiu, L. Cao, J. Huang, *Science* **2015**, *347*, 967; b) S. D. Stranks, G. E. Eperon, G. Grancini, C. Menelaou, M. J. P. Alcocer, T. Leijtens, L. M. Herz, A. Petrozza, H. J. Snaith, *Science* **2013**, *342*, 341; c) S. de Wolf, J. Holovsky, S.-J. Moon, P. Löper, B. Niesen, M. Ledinsky, F.-J. Haug, J.-H. Yum, C. Ballif, *J. Phys. Chem. Lett.* **2014**, *5*, 1035; d) NERL, 2017, https://www.nrel.gov/pv/assets/images/efficiency-chart.png, accessed: November 2017.

[3] a) L. Protesescu, S. Yakunin, M. I. Bodnarchuk, F. Krieg, R. Caputo, C. H. Hendon, R. X. Yang, A. Walsh, M. V. Kovalenko, *Nano Lett*. **2015**, *15*, 3692; b) E. R. Dohner, E. T. Hoke, H. I. Karunadasa, *J. Am. Chem. Soc*. **2014**, *136*, 1718; c) M. Saba, M. Cadelano, D. Marongiu, F. Chen, V. Sarritzu, N. Sestu, C. Figus, M. Aresti, R. Piras, A. Geddo Lehmann, C. Cannas, A. Musinu, F. Quochi, A. Mura, G. Bongiovanni, *Nat. Commun*. **2014**, *5*, 5049.

[4] G. Xing, N. Mathews, S. S. Lim, N. Yantara, X. Liu, D. Sabba, M. Grätzel, S. Mhaisalkar, T. C. Sum, *Nat. Mater*. **2014**, *13*, 476.

[5] a) F. Deschler, M. Price, S. Pathak, L. E. Klintberg, D.-D. Jarausch, R. Higler, S. Hüttner, T. Leijtens, S. D. Stranks, H. J. Snaith, M. Atatüre, R. T. Phillips, R. H. Friend, *J. Phys. Chem. Lett.* **2014**, *5*, 1421; b) S. D. Stranks, H. J. Snaith, *Nat. Nanotechnol*. **2015**, *10*, 391; c) H. Zhu, Y. Fu, F. Meng, X. Wu, Z. Gong, Q. Ding, M. V. Gustafsson, M. T. Trinh, S. Jin, X-Y. Zhu, *Nat. Mater*. **2015**, *14*, 636; d) S. A. Veldhuis, P. P. Boix, N. Yantara, M. Li, T. C. Sum, N. Mathews, S. G. Mhaisalkar, *Adv. Mater.* **2016**, *28*, 6804.

[6] a) M. U. Hassan, Y.-C. Liu, H. Butt, K. u. Hasan, J.-F. Chang, A. A. Olawoyin, R. H. Friend, *J. Polym. Sci. Part B: Polym. Phys.* **2016**, *54*, 15; b) Y. Kelestemur, B. Guzelturk, O. Erdem, M. Olutas, K. Gungor, H. V. Demir, *Adv. Funct. Mater.* **2016**, *26*, 3570.

[7] S. D. Stranks, S. M. Wood, K. Wojciechowski, F. Deschler, M. Saliba, H. Khandelwal, J. B. Patel, S. J. Elston, L. M. Herz, M. B. Johnston, A. P. H. J. Schenning, M. G. Debije, M. K. Riede, S. M. Morris, H. J. Snaith, *Nano Lett*. **2015**, *15*, 4935.

[8] Y. Tong, E. Bladt, M. F. Aygüler, A. Manzi, K. Z. Milowska, V. A. Hintermayr, P. Docampo, S. Bals, A. S. Urban, L. Polavarapu, J. Feldmann, *Angew. Chem. Int. Ed.* **2016**, *55*, 13887.

[9] a) J. You, Z. Hong, Y. Yang, Q. Chen, M. Cai, T.-B. Song, C.-C. Chen, S. Lu, Y. Liu, H. Zhou, Y. Yang, ACS Nano **2014**, *8*, 1674; b) Y. Li, L. Meng, Y. Yang, G. Xu, Z. Hong, Q. Chen, J. You, G. Li, Y. Yang, Y. Li, Nat. Commun. **2016**, *7*, 10214.

[10] J. A. Sichert, Y. Tong, N. Mutz, M. Vollmer, S. Fischer, K. Z. Milowska, R. G. Cortadella, B. Nickel, C. Cardenas-Daw, J. K. Stolarczyk, A. S. Urban, J. Feldmann, *Nano Lett*. **2015**, *15*, 6521.

[11] a) M. Yuan, L. N. Quan, R. Comin, G. Walters, R. Sabatini, O. Voznyy, S. Hoogland, Y. Zhao, E. M. Beauregard, P. Kanjanaboos, Z. Lu, D. H. Kim, E. H. Sargent, *Nat Nanotechnol.* **2016**, *11*, 872; b) X. Wu, M. T. Trinh, X. Y. Zhu, *J. Phys. Chem. C* **2015**, *119*, 14714; c) R. L. Milot, R. J. Sutton, G. E. Eperon, A. A. Haghighirad, J. M. Hardigree, L. Miranda, H. J. Snaith, M. B. Johnston, L. M. Herz, *Nano Lett.* **2016**, *16*, 7001.

[12] a) P. Müller-Buschbaum, *Adv. Mater.* **2014**, *26*, 7692; b) J. Schlipf, P. Docampo, C. J. Schaffer, V. Körstgens, L. Bießmann, F. Hanusch, N. Giesbrecht, S. Bernstorff, T. Bein, P. Müller-Buschbaum, *J. Phys. Chem. Lett*. **2015**, *6*, 1265; c) L. Oesinghaus, J. Schlipf, N. Giesbrecht, L. Song, Y. Hu, T. Bein, P. Docampo, P. Müller-Buschbaum, *Adv. Mater. Interfaces* **2016**, *3*, 1600403; d) P. Müller-Buschbaum, *European Polymer Journal* **2016**, *81*, 470; e) J. Schlipf, P. Müller-Buschbaum, *Adv. Energy Mater.* **2017**, 1700131.

[13] a) P. Docampo, F. C. Hanusch, N. Giesbrecht, P. Angloher, A. Ivanova, T. Bein, *APL Mater.* **2014**, *2*, 081508; b) N. Giesbrecht, J. Schlipf, L. Oesinghaus, A. Binek, T. Bein, P. Müller-Buschbaum, P. Docampo, *ACS Energy Lett.* **2016**, *1,* 150.

[14] a) H. Cho, S.-H. Jeong, M.-H. Park, Y.-H. Kim, C. Wolf, C.-L. Lee, J. H. Heo, A. Sadhanala, N. Myoung, S. Yoo, S. H. Im, R. H. Friend, T.-W. Lee, *Science* **2015**, *350*, 1222; b) J. H. Heo, D. H. Song, S. H. Im, *Adv. Mater.* **2014**, *26*, 8179–8183; c) B. Jiao, X. Zhu, W. Wu, H. Dong, B. Xia, J. Xi, T. Lei, X. Hou, Z. Wu, *Nanoscale* **2016**, *8*, 11084; d) J. Liang, Y. Zhang, X. Guo, Z. Gan, J. Lin, Y, Fan, X. Liu, *RSC Adv.* **2016**, *6*, 71070.

[15] a) J. H. Heo, D. H. Song, S. H. Im, *Adv. Mater.* **2014**, *26*, 8179; b) M. Saliba, K. W. Tan, H. Sai, D. T. Moore, T. Scott, W. Zhang, L. A. Estroff, U. Wiesner, H. J. Snaith, *J. Phys. Chem. C* **2014**, *118*, 17171.

[16] a) R.-J. Roe, *Methods of X-ray and Neutron Scattering in Polymer Science*, Oxford University Press, New York, USA **2000**; b) G. Beaucage, *J. Appl. Cryst.* **1996**, *29*, 134-146; c) D. Ma, A. D. Stoica, X.-L. Wang, *Nat. Mater.* **2009**, *8*, 30-34.

[17] a) H.-C. Liao, C.-S. Tsao, M.-H. Jao, J.-J. Shyue, C.-P. Hsu, Y.-C. Huang, K.-Y. Tian, C.-Y. Chen, C.-J. Sue, W.-F. Su, *J. Mater. Chem. A* **2015**, *3*, 10526; b) T. Miyadera, Y. Shibata, T. Koganezawa, T. N. Murakami, T. Sugita, N. Tanigaki, M. Chikamatsu, *Nano Lett.* **2015**, *15*, 5630.

[18] a) H. Frielinghaus, *Phys. Rev. E* **2007**, *76*, 051603; b) J.E. Martin, A.J. Hurd, *J. Appl. Cryst.* **1987**, *20*, 61-78.

[19] a) Y. Lin, J. A. Lim, Q. Wei, S. C. B. Mannsfeld, A. L. Briseno, J. J. Watkins, *Chem. Mater.* **2012,** *24*, 622-632; b) I. Tokarev, R. Krenek, Y. Burkov, D. Schmeisser, A. Sidorenko, S. Manko, M. Stamm, *Macromolecules* **2005**, *38*, 507-516; c) R. Wang, Z.-Y. Di, P. Müller-Buschbaum, H. Frielinghaus, *Polymer*, **2017**, *121*, 173.

[20] a) N. Kitazawa, D. Yaemponga, M. Aono, Y. Watanabe, *J. Lumin.* **2009**, *129*, 1036; b) S. Pathak, N. Sakai, F. Wisnivesky Rocca Rivarola, S. D. Stranks, J. Liu, G. E. Eperon, C. Ducati, K. Wojciechowski, J. T. Griffiths, A. A. Haghighirad, A. Pellaroque, R. H. Friend, H. J. Snaith, *Chem. Mater.* **2015**, *27*, 8066.

[21] a) G. C. Papavassiliou, I. B. Koutselas, *Synth. Met.* **1995**, *71*, 1713; b) P. Tyagi, S. M. Arveson, W. A. Tisdale, *J. Phys. Chem. Lett.* **2015**, *6*, 1911.

[22] a) C. de Weerd, L. Gomez, H. Zhang, W. J. Buma, G. Nedelcu, M. V. Kovalenko, T. Gregorkiewicz, *J. Phys. Chem. C* **2016**, *120*, 13310; b) N. Wang, L. Cheng, R. Ge, S. Zhang, Y. Miao, W. Zou, C. Yi, Y. Su, Y. Cao, R. Yang, Y Wei, Q. Guo, Y. Ke, M. Yu, Y. Jin, Y Liu, Q. Ding, D. Di, L. Yang, G. Xing, H. Tian, C. Jin, F. Gao, R. H. Friend, J. Wang, W Huang, *Nat. Photo.*, **2016**, *10*, 699.

[23] M. Xiao, F. Huang, W. Huang, Y. Dkhissi, Y. Zhu, J. Etheridge, A. Gray-Weale, U. Bach, Y.-B. Cheng, L. Spiccia, *Angew. Chem. Int. Ed.* **2014**, *53*, 9898.

[24] a) Z. Ning, X. Gong, R. Comin, G. Walters, F. Fan, O. Voznyy, E. Yassitepe, A. Buin, S. Hoogland, E. H. Sargent, *Nature* **2015**, *523*, 324; b) Z. Xiao, R. A. Kerner, L. Zhao, N. L. Tran, K. M. Lee, T.-W. Koh, G. D. Scholes, B. P. Rand, *Nat. Photonics* **2017**, *11*, 108.

[25] a) V. A. Hintermayr, A. F. Richter, F. Ehrat, M. Döblinger, W. Vanderlinden, J. A. Sichert, Y. Tong, L. Polavarapu, J. Feldmann, A. S. Urban, *Adv. Mater.* **2016***, 28*, 9478; b) Y. Tong, F. Ehrat, W. Vanderlinden, C. Cardenas-Daw, J. K. Stolarczyk, L. Polavarapu, A. S. Urban, *ACS Nano* **2016***, 10*, 10936.

[26] Heinz Maier-Leibnitz Zentrum. (2015). KWS-3: Very small angle scattering diffractometer with focusing mirror. *Journal of large-scale research facilities*, 1, A31. http://dx.doi.org/10.17815/jlsrf-1-28

[27] Forchungszentrum Jülich, Jülich Centre for Neutron Science, (2016). GALAXI: Gallium anode low-angle x-ray instrument. *Journal of large-scale research facilities*, 2, A61. http://dx.doi.org/10.17815/jlsrf-2-109

Table of Contents

Mixed dimensional hybrid perovskite thin films are prepared from a simple solution-processing route. Grazing incidence scattering (GIS) data statistically reveals that the development of thin film morphology as well as crystal orientation depends on the orientation of the organic component. The quality of amplified spontaneous emission (ASE) in perovskite films is demonstrated and appears to be closely correlated to the tailored morphology, highlighting its importance for realizing optical gain media.

Keywords: hybrid perovskite, amplified spontaneous emission, grazing incidence scattering, thin film

Rui Wang, Yu Tong, Aurora Manzi, Kun Wang, Zhendong Fu, Emmanuel Kentzinger, Jochen Feldmann, Alexander S. Urban*, Peter Müller-Buschbaum*, and Henrich Frielinghaus*

Preferential Orientation of Crystals Induced by Incorporation of Organic Ligands in Mixed-Dimensional Hybrid Perovskite Films

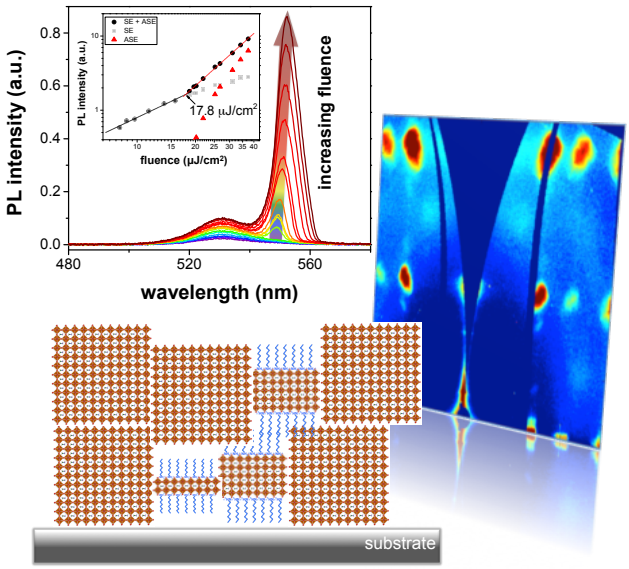

Supporting Information

Preferential Orientation of Crystals Induced by Incorporation of Organic Ligands in Mixed-Dimensional Hybrid Perovskite Films

Rui Wang, Yu Tong, Aurora Manzi, Kun Wang, Zhendong Fu, Emmanuel Kentzinger, Jochen Feldmann, Alexander S. Urban, Peter Müller-Buschbaum*, and Henrich Frielinghaus**

R. Wang, Dr. Z. Fu, Dr. H. Frielinghaus
Jülich Centre for Neutron Science at MLZ
Forschungszentrum Jülich GmbH
Lichtenbergstr. 1
85747 Garching, Germany
E-mail: h.frielinghaus@fz-juelich.de

Dr. E. Kentzinger
Jülich Centre for Neutron Science JCNS
Peter Grünberg Institut PGI
JARA-FIT
Forschungszentrum Jülich GmbH
52425 Jülich, Germany

Y. Tong, A. Manzi, Prof. J. Feldmann, Dr. A. S. Urban
Photonics and Optoelectronics Group
Department of Physics and Center for NanoScience (CeNS)
Ludwig-Maximilians-Universität München
Amalienstr. 54
80799 Munich, Germany
E-mail: urban@lmu.de

R. Wang, K. Wang, Prof. P. Müller-Buschbaum
Lehrstuhl für Funktionelle Materialien
Physik-Department
Technische Universität München
James-Franck-Str. 1
85748 Garching, Germany
E-mail: muellerb@ph.tum.de

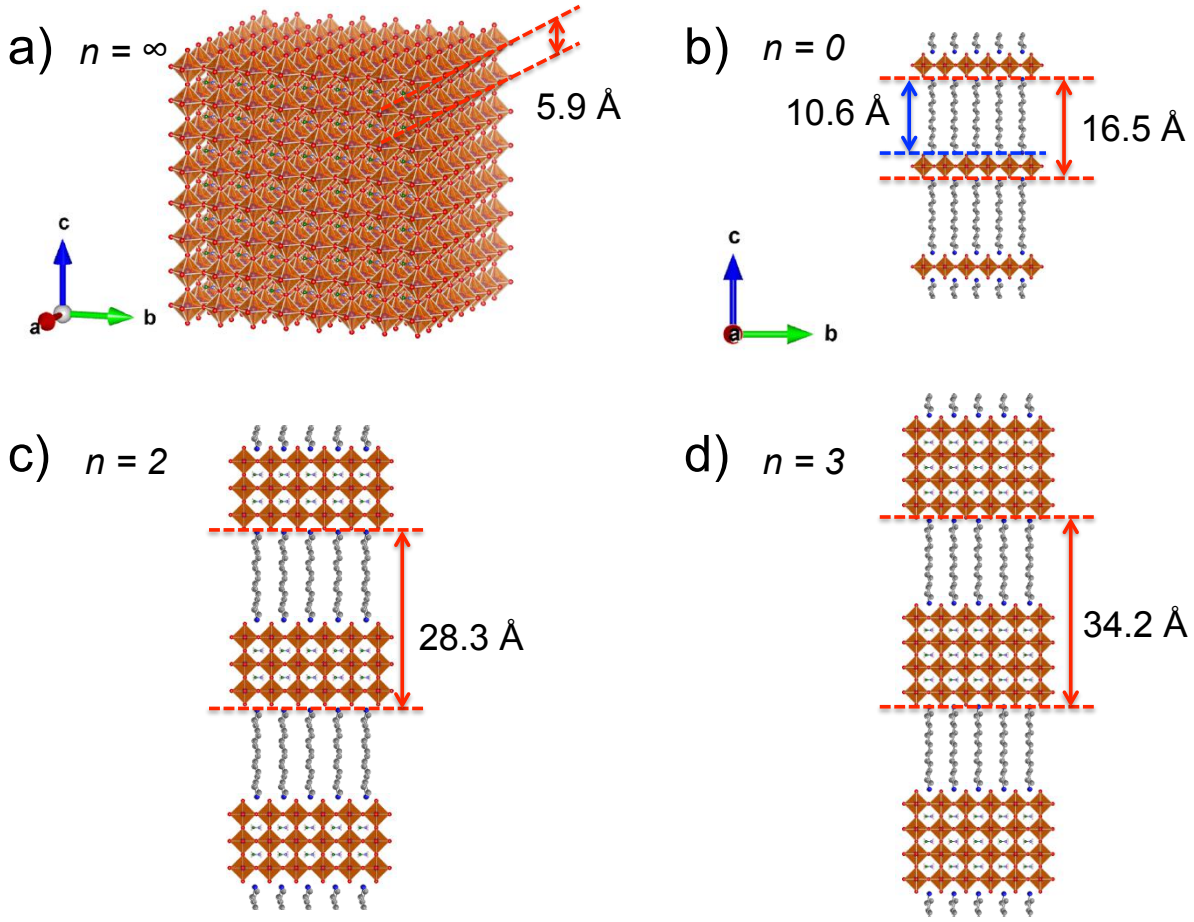

Figure S1. Schematic illustration of low dimensional perovskite platelets with different thickness: a) one single layer of $[PbBr_6]^{4-}$. b-d) different perovskite unit cell thickness (n) of 0, 2 and 3.

Table S1. Comparison of observed and reference values of 2D perovskite platelets thickness. We speculate the smaller value of the observed thickness compare to the theoretical value can be that the 2D platelets crystallites are compressed in the thin film geometry.

n_{Pb} [a)]	n_{Pero} [b)]	Theoretical thickness [Å]	Observed thickness [Å]
1	0	16.5	16.1
3	2	28.3	27.3
4	3	34.2	33.1

[a)] number of lead halide octahedral layers
[b)] number of complete perovskite unit cells

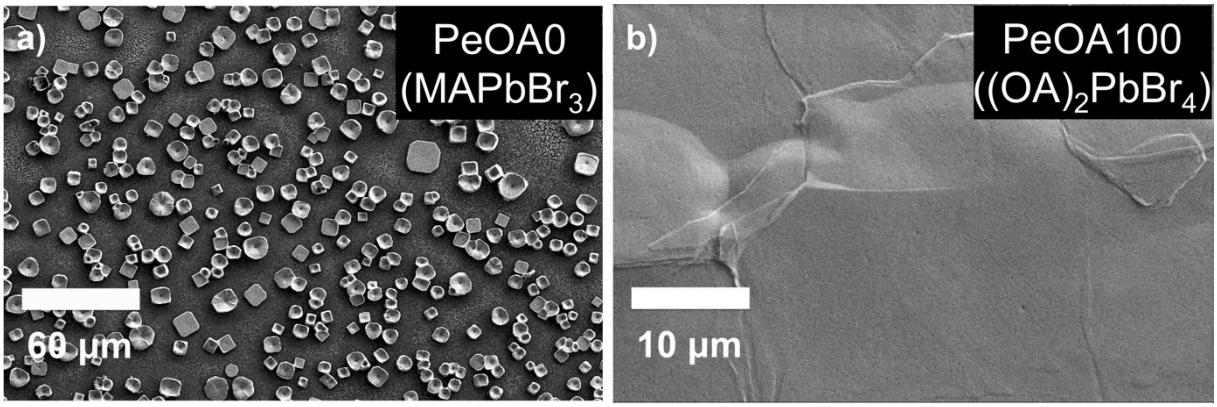

Figure S2. SEM top-view images of films prepared with a) 0 % and b) 100 % mole ratio of OABr. Sample with higher %OABr content tend to have good film-formation property with better surface coverage,[1] which supports our findings that perovskite crystal growth is constrained along the in-plane direction. However, no ASE behavior is observed for both samples.

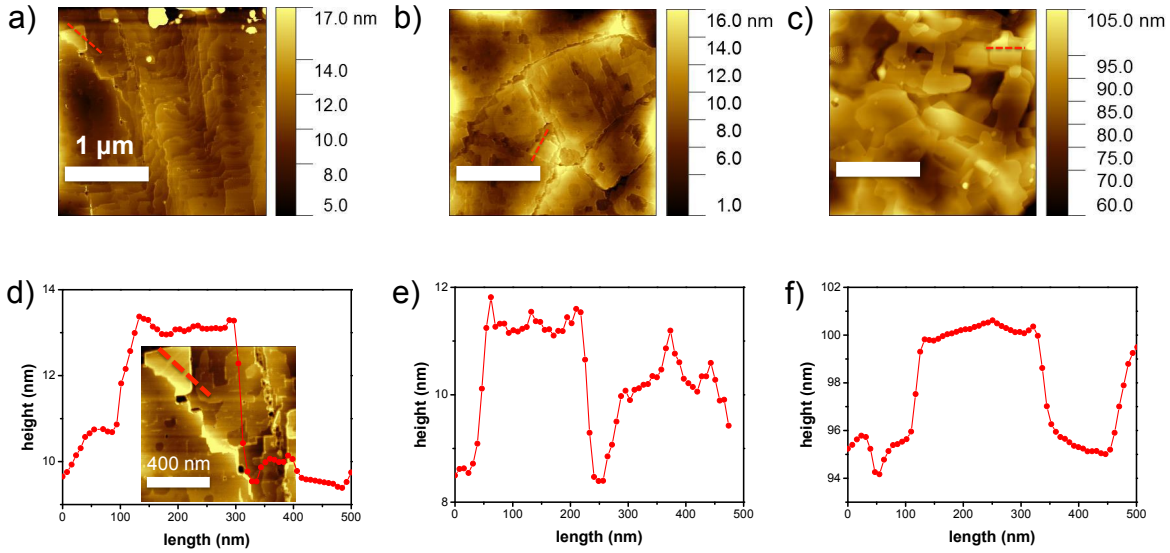

Figure S3. AFM topography images of perovskite films with varying mole ratio% of OABr: a) 10 % (PeOA10), b) 20 % (PeOA20) and c) 40 % (PeOA40). Line profiles of the AFM data taken at the marked positions for sample d) PeOA10, e) PeOA20 and f) PeOA40. The inset in panel d displays a bright 2D platelet structure at the left-top corner in the sample PeOA10.

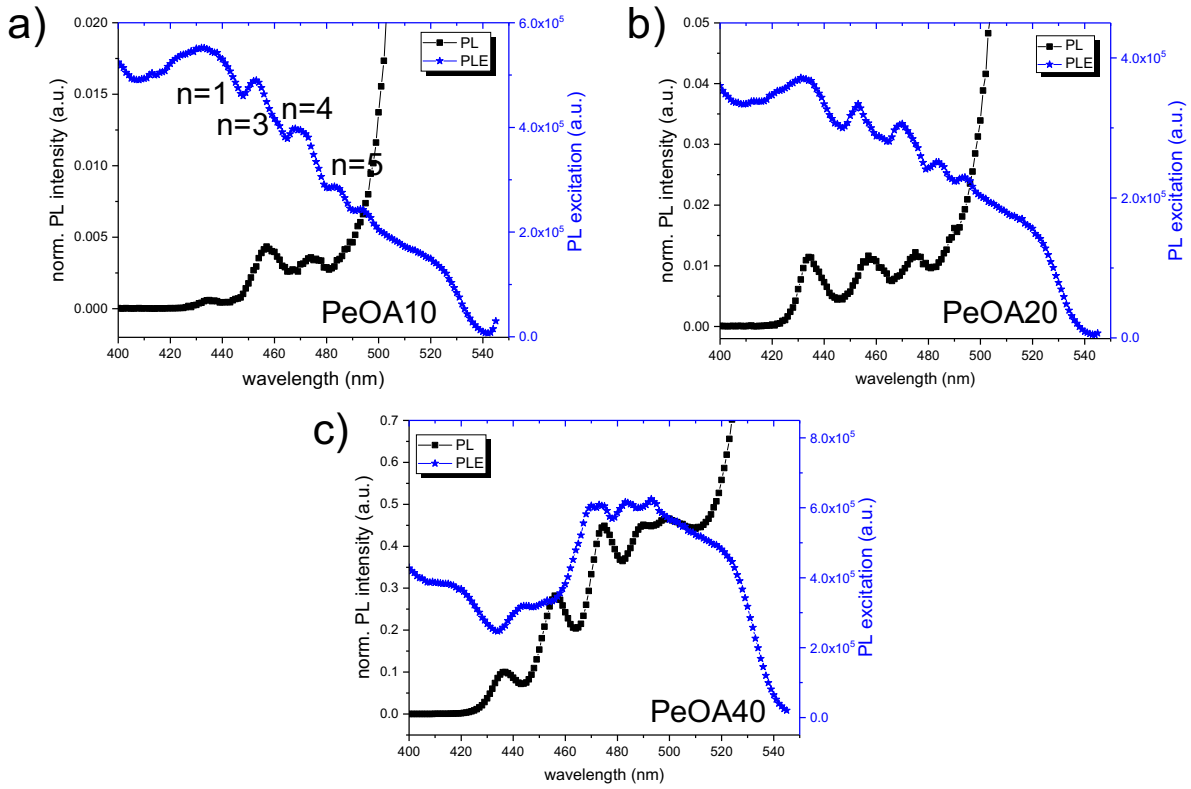

Figure S4. PL (black squares) and PLE (blue stars) spectra of sample a) PeOA10, b) PeOA20 and c) PeOA40. The low dimensional perovskite platelets are indexed in the PLE-spectrum in terms of $MAPbBr_3$ unit cell thickness (n).

GISANS fitting model and the resulting morphology parameters are shown in Figure S5. Data were analyzed in the framework of the distorted wave Born approximation (DWBA) using the local monodisperse approximation (LMA).[2] Three independent 1D cylinder-like paracrystals were used to represent the perovskite domains (Figure S5a). In the obtained results, perovskite domains gradually shrink at higher OABr content. In the meantime, the interspace distances (pore sizes) tend to increase, indicating the formation of a more porous network. An exceptive trend was observed in the pore size above 200 nm. Since a larger population of 2D perovskite platelets was observed in the sample PeOA40, this trend can result from the 2D domains aggregated stacking.

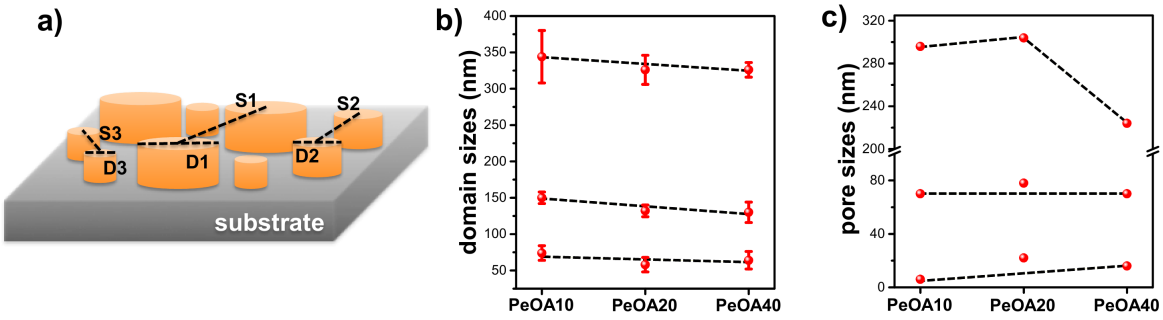

Figure S5. a) Schematic representation of applied GISANS model using 3 populations of cylinder-shaped objects. S and D respectively represent the structure factor and form factor used to describe each population. b-c) Morphology parameters of hybrid perovskite films with varying mole ratio% of OABr..

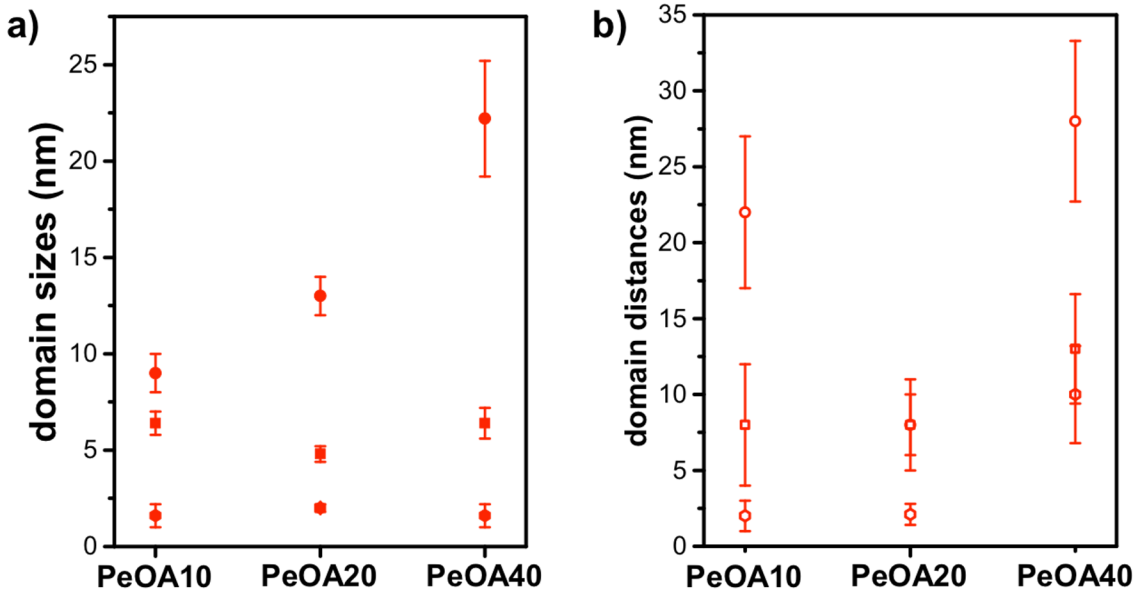

Figure S6. a-b) Morphology parameters obtained from GISAXS measurements of hybrid perovskite films with varying mole ratio% of OABr. The nanoscale domains above 7 nm are revealed to grow in sizes alongside the increasing of OABr content.

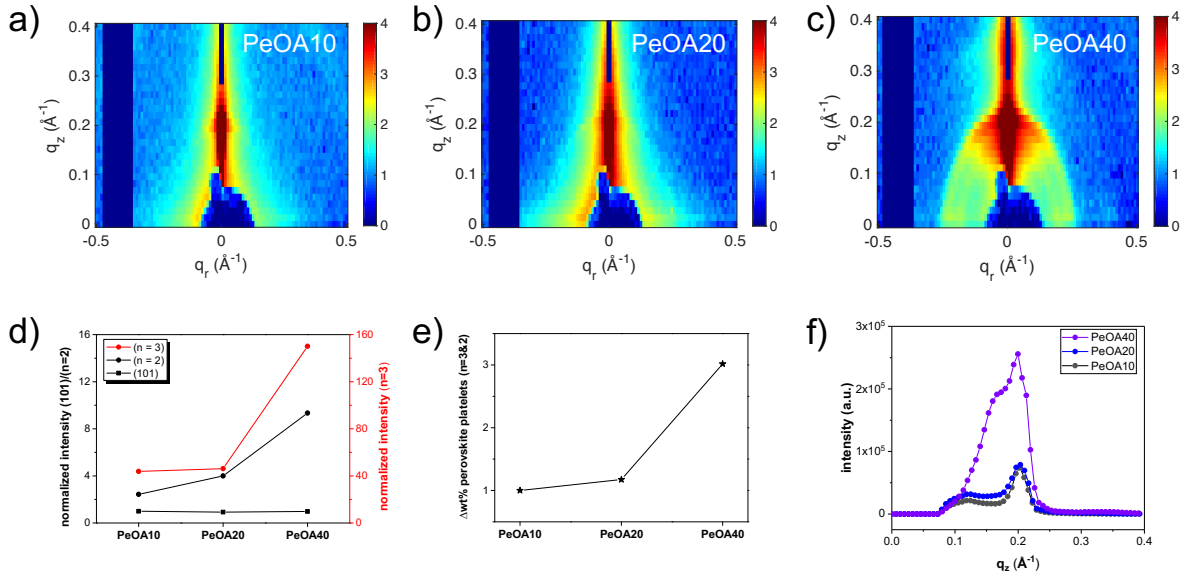

Figure S7. a-c) 2D GIWAXS data at $q \leq 0.4$ Å^{-1} of perovskite films with OABr mole ratio of 10% (PeOA10), 20% (PeOA20), and 40% (PeOA40). d) Normalized intensity integration of the (101) and the 2D platelets (n =3, 2) reflection peaks. e) Calculated amount variation for perovskite platelets in samples containing different OABr content. f) Vertical cuts at a q_r range of -0.02 Å^{-1} to 0.02 Å^{-1} for the three mixed-dimensional perovskite films. The Bragg peaks of 2D perovskite platelets are clearly visible below the missing wedge at $q_z = 0.19$ Å^{-1}, 0.23 Å^{-1}.

As seen in Figure S7, the 2D platelets at $q_z = 0.19$ Å^{-1}, 0.23 Å^{-1} are highly oriented in sample PeOA10 (Figure S7a) and sample PeOA20 (Figure S7b), whereas in sample PeOA40 (Figure S7c) additional intensities at an increasing range of azimuthal angles are observed. This result is identical to the findings from the 2D GISAXS data (Figure 4a-c), which implies that the 2D platelets orientation diversify at higher OABr content. The GIWAXS intensities are normalized to the (101) reflection peak of the sample PeOA10 in order to avoid problems induced by the inaccessible region and detector gaps. The normalization is carried out independently for each sample. Thereby, one can determine the amount of 2D perovskite platelets in the specific sample. The (101) Bragg peak in the GIWAXS data has contributions from both, 3D bulk crystals and quasi-2D platelets. Therefore, one can conclude that the total amount of crystals is relatively constant in the different perovskite films (Figure S7d). However, the amount of perovskite platelets increases by a factor of 2 in the sample PeOA40

compared to the sample PeOA10 (Figure S7e). As a consequence, the amount of 3D perovskite crystal decreases upon increasing the OABr content.

Figure S8 shows the photoluminescence decay data from the hybrid perovskite films. Data obtained from pure 3D $MAPbBr_3$ and 2D $(OA)_2PbBr_4$ platelets are shown as reference. Lifetimes are estimated by assessing the time it takes for the PL intensity to drop to 1/e of its original value. The PL lifetime is extended in sample PeOA10 in comparison to neat $MAPbBr_3$ film due to increased film continuity and full surface coverage (Figure 2c and Figure S2a). Whereas it decays faster upon further increasing OABr content, which is likely due to more trap states are included alongside the film morphology diversified.

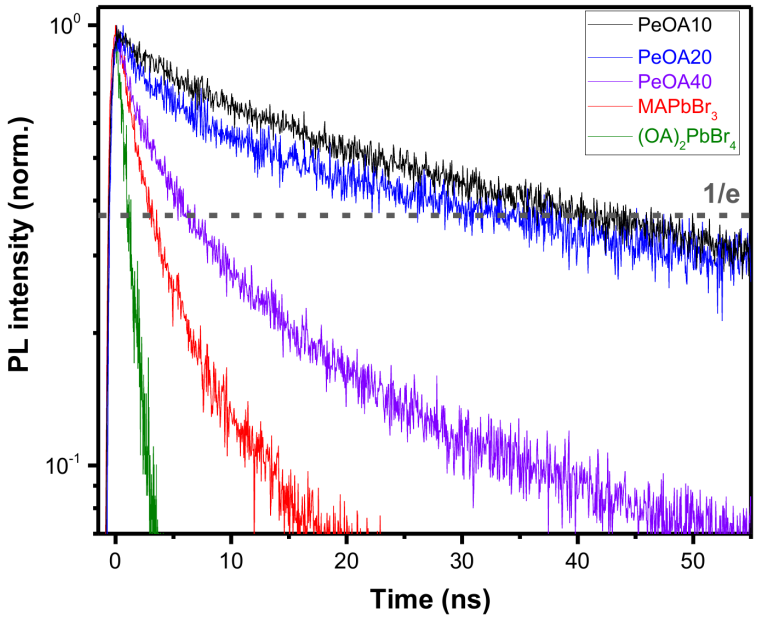

Figure S8. PL dynamics of hybrid perovskite films with varying mole ratio% of OABr. Data obtained from pure 3D $MAPbBr_3$ and 2D $(OA)_2PbBr_4$ platelets are shown as reference. In the mixed dimensional perovskite sample (PeOA10, PeOA20 and PeOA40) the lifetime ($\tau_{1/e}$) drops with increasing OABr content.

Table S2. Photoluminescence quantum yield (PLQY) and average PL lifetime ($\tau_{1/e}$) of perovskite films with varied OABr content.

	PeOA10	PeOA20	PeOA40
PLQY (%)	0.41	0.96	1.62
PL lifetime (ns)	41.2	36.7	6.3

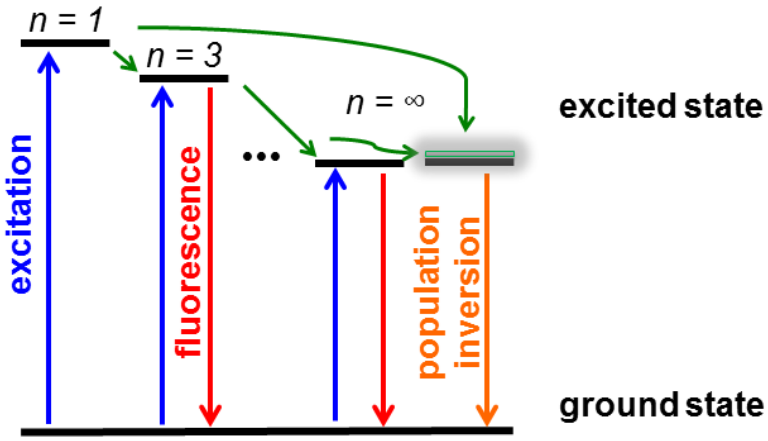

Figure S9. Schematic representation of the energy transfer in the multi-dimensional perovskite samples. Excitation energy is cascading funneled from smaller-n platelets into larger-n platelets, and further transferred to 3D bulk crystal.

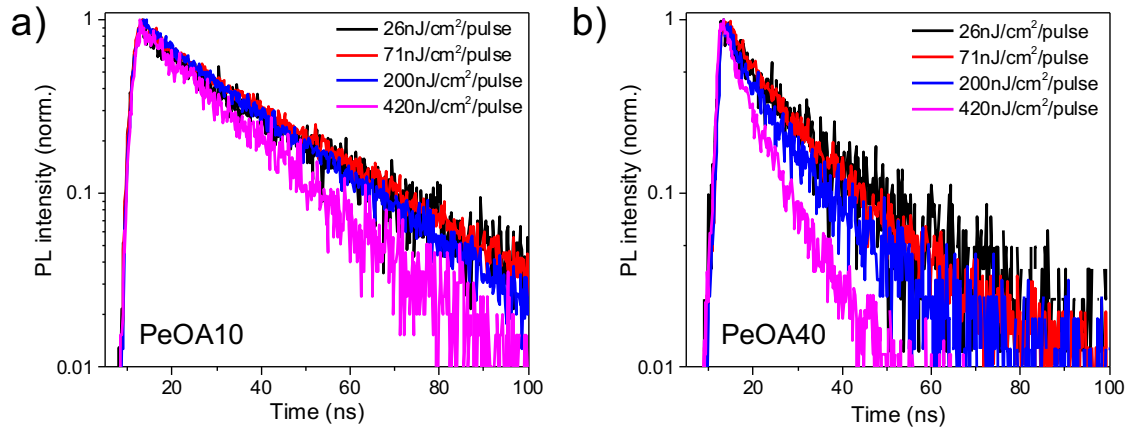

Figure S10. Power-dependent PL measurements for perovskite thin films a) PeOA10 and b) PeOA40. The applied excitation fluences are indicated in the images. The carrier concentration at the highest fluence (420 nJ/cm^2) is estimated to be on the order of 0.8-1.0 × 10^{17} cm^{-3}, which should suffice for enabling Auger recombination and is comparable to the value in literature.[3]

Supporting Information References

[1] D. B. Mitzi, K. Chondroudis, C. R. Kagan, *J. Res. Dev.* **2001**, *45*, 29.

[2] a) P. Müller-Buschbaum, *Anal. Bioanal. Chem.* **2003**, *376*, 3; b) R. Lazzari, *J. Appl. Cryst.* **2002**, *35*, 406.

[3] X. Wen, A. Ho-Baillie, S. Huang, R. Sheng, S. Chen, H.-c. Ko, M. A. Green, *Nano Lett.* **2015**, *15*, 4644.